Journal of Multiscale Modelling
Vol. 5, No. 4 (2013) 1350015 (24 pages)

DOI: 10.1142/S1756973713500157

Application of Multiscale Process Zone Model to Simulate Fracture in Polycrystalline Solids

Houfu Fan*, Chunxiang Shi*,† and Shaofan Li*,‡
*Department of Civil and Environmental Engineering
University of California, Berkeley, CA 94720, USA
†College of Urban Construction and Safety Engineering
Shanghai Institute of Technology, Shanghai 201418, P. R. China
‡shaofan@berkeley.edu

In this work, an early proposed atomistic-based multiscale process zone model is revised and employed to simulate crack propagation and spall fracture in polycrystalline solids. The multiscale process zone model is capable of describing heterogenous materials by incorporating the effect of inhomogeneities such as grain boundaries, slip lines and inclusions. A consistent depletion potential resulting from fundamental principles in colloidal physics is used to describe the cohesive laws for both the grain interfaces and process zones in bulk materials, which provides microstructure-based interface potentials in both normal and tangential directions with respect to finite element boundary separations in contrast to conventional cohesive methods. The polycrystalline microstructure are generated by using the Voronoi tessellations. Two different approaches of treating the process zone are proposed. The multiscale process zone model is implemented in a Lagrange framework based on the Galerkin weak form formulation. In addition, to eliminate the zero-energy modes and avoid shear locking in the interphase elements, a reduced integration technique is adopted in simulations. Numerical simulations on crack propagation in materials with various cohesive strengths have been carried out, and they can describe both inter-granular and trans-granular fractures. Finally, the spall-fracture of a specimen under high-impact load is captured using the proposed multiscale process zone model.

Keywords: Process zone model; crack; fracture; multiscale simulation; polycrystalline solids.

1. Introduction

Polycrystalline materials like metals, alloys or ceramics are of great importance in materials science and engineering. Most common structural materials like ceramics and metals or alloys are in polycrystalline form in which each grain has a unique crystallographic orientation, shape, and size, and each of them has a direct effect on

---

‡Corresponding author.

local or global mechanical properties. To model the mechanical behavior of polycrystalline solids, researchers have developed methods based on theories at various scales, ranging from Quantum Mechanical (QM), classical Molecular Dynamics (MD), Monte Carlo simulation (MC) to Geometrical Models (GM) and Continuum Mechanics (CM).[1] For instance, *ab-initio* calculations (based on QM) are used to design BCC Mg-Li alloys for ultra-lightweight applications.[2] MD simulations have been used to investigate the transition with decreasing size from a dislocation-based to a grain-boundary based mechanism of nanocrystalline metals.[3] With a three-dimensional MC model, recrystallization and grain growth are studied.[4] These methods at nano/micro scale are very useful in uncovering certain new features or mechanisms at very small size, but they are in general limited to the length and time scales. For practical applications, one should consider methods at macro level, which mainly consists of two different types of methods: the classical continuum damage model[5–8] and the cohesive finite element method.[9–13] For example, a temperature dependent creep damage model is developed to study the damage in polycrystalline ice.[14] Void growth of polycrystalline solids is studied based on an extension of the continuum damage model.[15] Constitutive theory for brittle to damage of polycrystalline materials under dynamic loading is developed based on a continuum damage model that incorporates several microscale damage mechanisms.[16] A nonlocal cohesive zone model for finite thickness interfaces is applied to polycrystalline solids.[17] The interplay between cohesive cracking and plasticity in polycrystal solids is investigated by a three-dimensional cohesive zone model.[18] Meanwhile, there are also some other multiscale methods in the simulation of material damage or fracture. For instance, a multiscale boundary element method is developed to study material degradation and fracture.[19] A hierarchical multilevel method is developed for plastic deformation of polycrystalline materials, which consists of macroscopic models of which the parameters have to be identified through a sub level.[20]

In this work, we are focusing on the multiscale process zone method, because that the classical continuum damage models do not contain the lattice orientations of constitutive grains and other related information at microscale. The multiscale process zone method used in this work is different from the cohesive zone model developed by Xu and Needleman.[9] In that model, a so-called cohesive zone is embedded along the edge between two bulk elements. which acts as a ‘glue’. An empirical surface of traction-displacement relation is adopted in the cohesive zone. By doing so, stress singularity can be avoided. Moreover, the crack initiation or propagation does not rely on any artificial criterion but a natural outcome of simulations.

One obvious drawback of the conventional cohesive zone FEM is that the constitutive relations in the bulk element and in the cohesive zone are disjointed, to certain degree. Aside from the fact that the traction-displacement relation is empirical, separate normal and tangential cohesive laws are also prescribed. This empirical cohesive laws can easily reach its limit of sub-micron scale due to the high size-dependence of plasticity at small scale. Ideally a good cohesive zone model should be directly built on the mesoscale cohesive potential. In principle, the exact mesoscale cohesive potential is to be derived from the atomistic potential based on a first-principle calculation.

To resolve this problem, Zeng and Li took a completely different approach,[21] by proposing a multiscale cohesive zone model or the multiscale process zone model. In the model proposed, both the bulk constitutive relation and the cohesive laws are constructed based on the atomistic potential, which naturally takes into account the information of lattice microstructure such as atom position and lattice orientation. Two scale of coarse graining are considered in this model, one for the bulk medium and the other for the material interfaces. In both the bulk element and the cohesive zone of finite width, the Cauchy-Born rule is used to describe the corresponding deformations inside. The multiscale process zone model has been applied to solve many practical problems. For instance, Zeng and Li employed the method to model composites.[22] He and Li proposed a multiscale embedded atom cohesive process zone finite element model to simulate fracture and crack propagations.[23] Liu and Li proposed a finite temperature multiscale interphase zone model to study fracture process of metallic materials at finite temperature.[24] More importantly, Qian and Li have used the multiscale process zone model to study fracture in polycrystalline solids.[25] A review of the process zone model and its applications in fracture can be found in Ref. 26.

In this work, the application of the multiscale process zone model to fracture of polycrystalline solids is revisited. There are several differences between the current work and that in Ref. 25. In the original work of Qian and Li,[25] the deformation inside the process zone is assumed to be homogeneous, and a special depletion potential is used to derive the constitutive model inside the process zone; whereas in the present work, to account for the highly nonuniform deformation in the process zone, two different approaches are implemented. In the first approach, a reduced two point integration is employed to obtain the traction force resulting from the process zone, as what has been proposed by Li.[26] Although the regular first order Cauchy-Born rule is still employed to derive the constitutive relation (i.e, the deformation is assumed to be uniform at each Gauss integration point), the overall deformation in the process zone is in general nonuniform. In the second approach, the deformation inside the process zone is assumed to be inhomogeneous and nonlinear, and the second order Cauchy-Born rule or a strain gradient Cauchy-Born rule is employed to derive constitutive relation in order to accommodate the nonuniform deformation inside the process zone.

The multiscale process zone model is implemented in a Lagrange type of the Galerkin finite element weak form formulation. Reduced integrations are employed to eliminate the zero-energy modes and avoid shear lockings in the cohesive elements. Numerical simulations on crack propagations with various cohesive strengths that govern the fracture path (inter-granular or trans-granular) are carried out, using the two different approaches. By comparing the corresponding crack surface morphologies with that of the normally used assumption that the deformation is uniform in the cohesive zone, it is shown that the proposed approaches are better in terms of numerical performances. Meanwhile, using a series of consecutive refinements of am uniaxial tension model, it is revealed that the proposed model is size-independent in terms of the crack propagation along the grain boundaries. Finally the spall-fracture of a specimen under high-impact load is successfully captured using the proposed multiscale process zone model.

This paper is organized into five sections. We first present the modeling of the polycrystalline structure in Sec. 2. In Sec. 3, the detail of the multiscale process zone model is provided. The Galerkin weak form and corresponding implementation is offered in Sec. 4. Several numerical examples are presented in Sec. 5. We close our presentation by making a few remarks in Sec. 6.

2. Polycrystalline Microstructure

A polycrystalline solid consists of many grains of different size, shape and crystallographic orientation. In this work, the voronoi tessellations are used to generate different randomly shaped microstructure in order to study the effect of polycrystalline grain morphology, which has been studied by many researchers.[13,27,28] As shown in Fig. 1(a), each Voronoi cell represents a grain and the edge between two neighboring cells is considered as the grain boundary. Inside each grain, triangle elements are generated using the method of delaunay triangulation. All the elements in the grains are treated as the bulk elements. In the cohesive Finite Element Method, cohesive zones are always needed such that one can link two bulk elements. In a way, a cohesive zone can be viewed as a "glue" for the corresponding bulk elements. As can be seen from Fig. 1(b), the triangular meshes are conforming between adjacent grains, which is important because that cohesive zones are not only built up as the interface zones in the bulk, but also those along the grain edges. If the triangular meshes between two neighboring grains are not consistent,

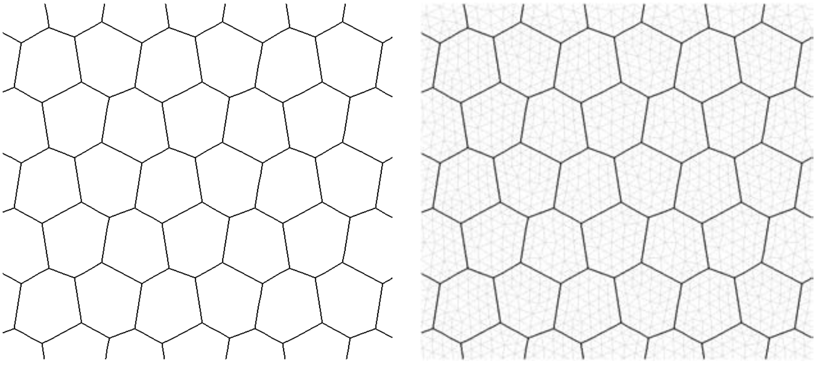
(a) (b)

Fig. 1. Mesh generation: (a) Voronoi cell. (b) Triangular bulk elements over grains.

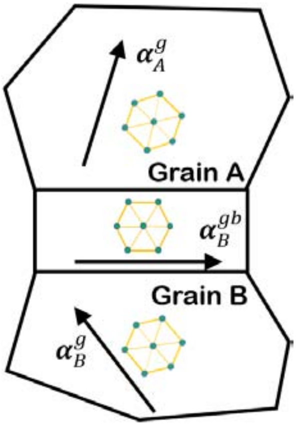

Fig. 2. Orientation of grains and grain boundary.

then one would encounter difficulties in generating the cohesive zones along the corresponding edge.

From microscale perspectives, each grain has its unique orientation. In this work, each grain is randomly assigned a lattice orientation α^g, indicating that all the bulk elements and the process zones in one grain share the same lattice orientation. Notice that the superscript g represents granular region and the superscript gb denotes the zones on grain boundaries. In addition, the lattice orientation of grain boundary zones α^{gb} may be assigned according to various principles or assumptions. For the sake of simplicity, the lattice orientation of a grain boundary zone is chosen to be the average of orientations from the two adjacent grains, i.e., $\alpha^{gb} = \frac{1}{2}(\alpha_A + \alpha_B)$, as shown in Fig. 2.

Other than the lattice orientation, another important factor for the constitutive relations in the process zones is the magnitude of the depletion potential. Different scenarios regarding the relative strength between the depletion potential in the process zones in the grain and that along the grain boundaries are considered in the simulation.

3. A Multiscale Process Zone Model

The multiscale process zone model (MPZM) is a generic coarse grain model based on the atomistic information of the lattice structure, which provides the constitutive modeling for process zones among bulk elements. In the MPZM, a global nonuniform deformation field can be viewed as macroscale piecewise uniform deformation fields inside the bulk elements of uniformed deformations, connected by finite-width process zones with highly nonuniform deformations. Making use of the lattice structure, orientation and the inter-atomic interaction potential, the effective constitutive properties in bulk elements can be modeled by the Cauchy-Born rule, as shown in Fig. 3(a). To better characterize the highly nonuniform deformations

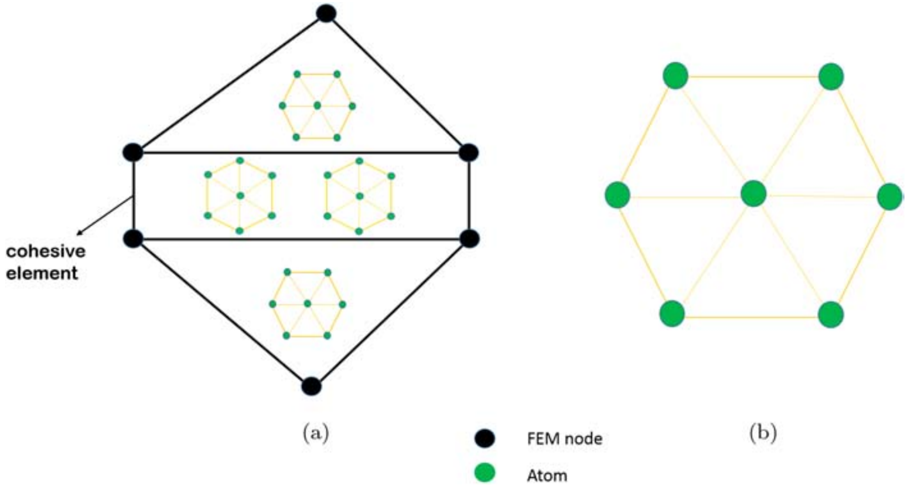

Fig. 3. Multiscale process zone model: (a) Triangular bulk element and cohesive zone. (b) Hexagonal lattice used in this paper.

inside the cohesive zones, in this work, we propose to use the second order Cauchy-Born rule in these regions. Two different approaches in treating the finite-width process zones are proposed. In the first approach, the stresses at the Gauss integration points inside the cohesive zone are calculated using the first order Cauchy-Born rule. Through a two point reduced integration, one can obtain the corresponding traction vectors, which are further integrated along the process zone to obtain the finite element nodal forces for the corresponding bulk elements. In the second approach, a process zone is viewed as a four-node quadrilateral element, where the four nodes are coming from that of the adjacent bulk elements. Importantly, to account for the severe nonlinearity in the process zone, the stresses at the Gauss integration points are obtained using the second order Cauchy-Born rule, which are then integrated to obtain the resulting nodal forces. In both approaches, the coarse grain model for the process zone is properly connected with the kinematics of bulk elements. It can be seen that using the proposed approaches, the effective deformation field inside the process zones can be uniquely determined by the bulk finite element nodal displacements. In addition, the MPZM eliminates the discontinuous jump operator approach in description of the displacement field required in the traditional cohesive finite element method.

In this work, the following 12-6 Lennard-Jones potential is used to describe the inter-atomic potential of lattice in the bulk element

$$\phi_{bulk} = 4\epsilon\left[\left(\frac{\sigma}{r}\right)^{12} - \left(\frac{\sigma}{r}\right)^{6}\right]. \tag{1}$$

Compared to the bulk element, the process zone is a relatively weak interface, where slip lines, inclusions and dislocations usually reside. A so-called depletion potential[29] can be derived for the highly inhomogeneous deformation field inside the process zone. The depletion potential can be viewed as a genetic enrichment from the underneath atomistic structure. In fact, if we assume that the process zone is a compliance interface that is much weaker than the adjacent bulk elements, and the intermolecular interaction inside the cohesive zone is long-range like the Van der Waals interaction between noncovalent bonds or quasi-covalent bonds, the depletion potential can be obtained by integrating the bulk atomistic potential over the rigid bulk medium half space. For instance, corresponding to the bulk potential in Eq. (1), the depletion potential can be derived as,

$$\phi_{\text{depl}}(r) = \int_{\text{Half Space}} \beta\phi_{\text{bulk}}(r - r')dV' = \frac{\pi\epsilon}{\sqrt{2}}\left(\frac{1}{45}\left(\frac{r_0}{r}\right)^9 - \frac{1}{3}\left(\frac{r_0}{r}\right)^3\right), \tag{2}$$

where β is the atomic density, ϵ the depth of the potential well, σ the finite distance at which the bulk atomistic potential is zero, and $r_0 = 2^{1/6}\sigma$ the equilibrium bond distance in the bulk. In this way, we obtained a closed-form expression of the interface depletion potential for the cohesive zone.

3.1. *Constitutive relations in the bulk*

In order to reduce the complexity in describing the bulk atomistic potential based on the lattice model, the first order Cauchy-Born rule is adopted. Consider a two-dimensional lattice model consists of multiple cells with the six-node hexagon being the basic unit cell. (see Fig. 3(b)). Each hexagon unit has six nearest bonds $\mathbf{R}_i$, $i = 1, n_b$, $n_b = 6$. Based on the first-order Cauchy-Born rule, the bulk element deformation is uniform. Thus the deformed bond $\mathbf{r}_i$ can be related to the undeformed bond $\mathbf{R}_i$ by a constant tensor $\mathbf{F}_e$, i.e., $\mathbf{r}_i = \mathbf{F}_e \cdot \mathbf{R}_i$. This constant tensor $\mathbf{F}_e$ is the averaged deformation gradient with this bulk element. Consequently, the strain energy density function in each bulk element can be written as

$$W_e = \frac{1}{2\Omega_0^b}\sum_{i=1}^{n_b}\phi(r_i(\mathbf{F}_e)) = W_e(\mathbf{F}_e), \tag{3}$$

where superscript b indicates bulk element, Ω_0^b is the volume of the unit cell in the referential configuration, $\phi(r_i)$ is the atomistic potential, $r_i, i = 1, 2, \ldots, n_b$ are the current bond lengths in a unit cell. Notice that in Eq. (3) there is a factor of $\frac{1}{2}$ in the front, this is because that the potential energy $\phi(r_i)$ is always shared by two atoms. With the strain energy density function, the constitutive relations for the bulk medium can be readily established. For instance, the first Piola-Kirchhoff stress $\mathbf{P}$ can be written in the following form:

$$\mathbf{P} = \frac{\partial W_e}{\partial \mathbf{F}_e} = \frac{1}{2\Omega_0^b}\sum_{i=1}^{n_b}\frac{\partial\phi}{\partial r_i}\frac{\mathbf{r}_i \otimes \mathbf{R}_i}{r_i}. \tag{4}$$

Once $\mathbf{P}$ is determined, one can easily substitute it into the Galerkin weak form (see Sec. 4) and perform the related computation.

3.2. *Multiscale modeling of the process zone*

Due to the highly nonuniform deformation inside the process zone, the conventional Cauchy-Born rule is not suitable to be directly employed. Instead, we turn our attention to the second order Cauchy-Born rule, in which a deformed bond vector $\mathbf{r}_i$ is expressed as

$$\mathbf{r}_i = \mathbf{F}_c \cdot \mathbf{R}_i + \frac{1}{2}\mathbf{G}_c : (\mathbf{R}_i \otimes \mathbf{R}_i), \tag{5}$$

where the $\mathbf{G}_c$ is the derivative of the deformation gradient

$$\mathbf{G}_c = \frac{\partial \mathbf{F}_c}{\partial \mathbf{X}} = \frac{\partial^2 \mathbf{x}}{\partial \mathbf{X} \otimes \partial \mathbf{X}}. \tag{6}$$

The subscript c indicates the quantity is defined within the cohesive or process zone. Using the depletion potential in Eq. (2), and assuming the basic hexagon unit cell (in the reference configuration) in the process zone, the corresponding strain energy density function can be written as

$$W_c = \frac{1}{2\Omega_0^c} \sum_{i=1}^{n_b} \phi_{depl}(r_i(\mathbf{F}_c)) = W_c(\mathbf{F}_c, \mathbf{G}_c). \tag{7}$$

Notice that W_c is a function of $\mathbf{F}_c$ and $\mathbf{G}_c$. To characterize the internal virtual work, in addition to the first Piola-Kirhhoff stress $\mathbf{P}_c$, a higher order stress couple $\mathbf{Q}_c$ is defined within the process zone. The mathematical expressions for the two stresses are

$$\mathbf{P}_c = \frac{\partial W_c}{\partial \mathbf{F}_c} = \frac{1}{2\Omega_0^c} \sum_{i=1}^{n_c} \frac{\partial \phi_{depl}}{\partial r_i} \frac{\mathbf{r}_i \otimes \mathbf{R}_i}{r_i}, \tag{8}$$

$$\mathbf{Q}_c = \frac{\partial W_c}{\partial \mathbf{G}_c} = \frac{1}{2\Omega_0^c} \sum_{i=1}^{n_c} \frac{\partial \phi_{depl}}{\partial r_i} \frac{\mathbf{r}_i \otimes \mathbf{R}_i \otimes \mathbf{R}_i}{r_i}. \tag{9}$$

As can be seen, the modeling of the process zone requires the computation of both the deformation gradient $\mathbf{F}_c$ and the derivative of the deformation gradient $\mathbf{G}_c$. It seems very challenging to obtain the above two quantities out of a finite width zone sandwiched by two triangle elements. For the FEM mesh considered here, we can always view the process zone as a four-node quadrilateral element (see Fig. 4), in which the two nodes on the top and two on the bottom come from the adjacent triangle bulk elements. Using the standard four-node isoparametric FEM, one can obtain

$$\mathbf{F}_c = \mathbf{I} + \frac{\partial \mathbf{N}}{\partial \mathbf{X}} \cdot \mathbf{d} \tag{10}$$

and

$$\mathbf{G}_c = \frac{\partial^2 \mathbf{N}}{\partial \mathbf{X} \otimes \partial \mathbf{X}} \cdot \mathbf{d}, \tag{11}$$

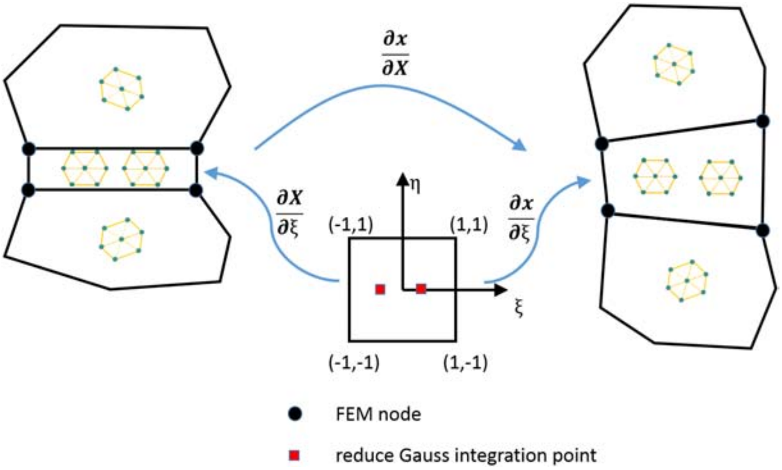

Fig. 4. Schematic in treating the cohesive zone as a four-node quadrilateral element.

where **I** is the second-order identity matrix, **N** is the FEM shape functions and **d** denotes the nodal displacements. For details on the isoparametric shape functions, their derivatives, the reader may consult Ref. 30.

In addition to the second order Cauchy-Born rule, one can also distribute multiple Gauss integration points inside the process zone element, such that the highly nonuniform deformation is better captured. Compared to the conventional four-node quadrilateral element, the process element has a very small width, which has its pros and cons in real applications. On one hand, it can easily lead to shear locking, which requires special techniques (such as reduced integration) in computations. In this work, the 2×1 integration scheme is adopted, which is believed to be the minimum number of Gauss integration points needed to eliminate the associated zero-energy modes, especially the hour-glass mode. On the other hand, instead of following the conventional FEM procedure to obtain the finite element nodal forces, it enables us to directly treat the top and bottom surface as the boundaries of the corresponding bulk elements. This means that one can first obtain the stresses in the process zone, and then the traction forces on the two boundaries, which are further integrated to obtain the nodal forces. Nevertheless, the two approaches in treating the process zone are both implemented in the current work.

3.2.1. *The first approach*

As shown in Fig. 4, we first obtain the first Piola-Kirchhoff stress $\mathbf{P_c}$ at the two Gauss integration points using Eq. 8. In the first approach, for each Gauss integration point, one can obtain the traction force at the top and bottom boundary using

$$\mathbf{T} = \mathbf{P} \cdot \mathbf{N}, \tag{12}$$

where $\mathbf{N}$ is the unit out normal of the triangle element at the corresponding boundary in the reference configuration. Integrating over the boundary, one can obtain

$$\mathbf{f}_{ct} = cL\mathbf{T}, \tag{13}$$

where cL denotes the length of the process zone. This resultant force $\mathbf{f}_T$ needs to be distributed onto the two nodes of the corresponding boundary,

$$\mathbf{f}_1 = \mathbf{f}_{ct}N_1; \quad \mathbf{f}_2 = \mathbf{f}_{ct}N_2, \tag{14}$$

where N_1 and N_2 are the FEM shape functions of the two nodes, evaluated at the corresponding Gauss integration point. Note that in this approach, the information from the high order stress $\mathbf{Q}_c$ is not included.

3.2.2. *The second approach*

In the second approach, the contribution of the process zone element is accommodated through the standard FEM prodedure. Consider the first variation of the internal strain energy in the process zone element

$$\delta W_c = \int_{\Omega_c} \left(\mathbf{P}_c : \delta\mathbf{F}_c + \mathbf{Q}_c \,\vdots\, \delta\mathbf{G}_c \right) dv. \tag{15}$$

Substituting the FEM displacement interpolation $\mathbf{u} = \mathbf{N}\mathbf{d}$ and its variation $\delta\mathbf{u} = \mathbf{N}\delta\mathbf{d}$ into Eq. (15), and with some standard manipulation, one can obtain the resulting nodal force vectors of the process zone elements as

$$\mathbf{f}_{ce} = \int_{\Omega_{c0}} \left(\mathbf{P}_c \cdot \frac{\partial\mathbf{N}}{\partial\mathbf{X}} + \mathbf{Q}_c : \frac{\partial^2\mathbf{N}}{\partial\mathbf{X}\otimes\partial\mathbf{X}} \right) dV. \tag{16}$$

In practical application, the above integration is replaced with finite summation over the two Gauss integration points.

4. FEM Implementations

Based on the two different approaches in treating the process zone, the Galerkin weak form of the multiscale process zone model can be written as (the first approach —(17), and the second approach — (18))

$$\begin{aligned} &\sum_{e=1}^{n^b_{elem}} \left\{ \int_{B_0^e} \rho_0 \ddot{\boldsymbol{\varphi}}^h \cdot \delta\boldsymbol{\varphi}^h dV + \int_{B_0^e} \mathbf{P}(\boldsymbol{\varphi}) : \delta\mathbf{F}^h dV - \int_{S_c^e} \mathbf{T}^{cohe} \cdot \delta\boldsymbol{\varphi}^h dS \right\} \\ &\quad = \sum_{e=1}^{n^b_{elem}} \left\{ \int_{B_0^e} \mathbf{B} \cdot \delta\boldsymbol{\varphi}^h dV \right\} + \int_{\Gamma_t} \mathbf{T}^{cohe} \cdot \delta\boldsymbol{\varphi}^h dS, \end{aligned} \tag{17}$$

or

$$
\begin{aligned}
&\sum_{e=1}^{n^b_{elem}} \left\{ \int_{B^e_0} \left[\rho_0 \ddot{\boldsymbol{\varphi}}^h \cdot \delta \boldsymbol{\varphi}^h + \mathbf{P}(\boldsymbol{\varphi}) : \delta \mathbf{F}^h \right] dV \right\} \\
&\qquad + \sum_{e=1}^{n^c_{elem}} \left\{ \int_{C^e_0} \left[\mathbf{P}(\boldsymbol{\varphi}) : \delta \mathbf{F}^h + \mathbf{Q}(\boldsymbol{\varphi}) \,\vdots\, \delta \mathbf{G}^h \right] dV \right\} \\
&\quad = \sum_{e=1}^{n^b_{elem}} \left\{ \int_{B^e_0} \mathbf{B} \cdot \delta \boldsymbol{\varphi}^h dV \right\} + \sum_{e=1}^{n^c_{elem}} \left\{ \int_{C^e_0} \mathbf{B} \cdot \delta \boldsymbol{\varphi}^h dV \right\} + \int_{\Gamma_t} \mathbf{T} \cdot \delta \boldsymbol{\varphi}^h dS,
\end{aligned}
\tag{18}
$$

where B^e_0 represents the domain of a bulk element, C^e_0 is the domain of a process zone element, Γ_t is the traction boundary of the system, and $S^e_c := \partial B^e_0 / \partial_t B^e_0$. Notice that in the above weak form, the mass of the process zone element is omitted, because they are of very small width compared to the bulk element.

Consider following FEM interpolations,

$$
\mathbf{u}^h(\mathbf{X}) = \sum_{I=1}^{n_{node}} N_I(\mathbf{X}) \mathbf{d}_I .
$$

Following the standard FE discretization procedure, one can obtain the following discrete equations of motion

$$
\mathbf{M}\ddot{\mathbf{d}} + \mathbf{f}^{int}(\mathbf{d}) + \mathbf{f}^{cohe}(\mathbf{d}) = \mathbf{f}^{ext}, \tag{19}
$$

where

$$
\begin{aligned}
\mathbf{M} &= \mathop{\boldsymbol{A}}_{e=1}^{n^b_{elem}} \int_{B^e_0} \rho_0 \mathbf{N}^{eT} \mathbf{N}^e dV \\
\mathbf{f}^{int} &= \mathop{\boldsymbol{A}}_{e=1}^{n_{elem}} \int_{B^e_0} \mathbf{B}^{eT} \mathbf{P}^e(\mathbf{d}) dV \\
\mathbf{f}^{ext} &= \mathop{\boldsymbol{A}}_{e=1}^{n_{elem}} \left\{ \int_{B^e_0} \mathbf{N}^{eT} \mathbf{B}^e dV + \int_{\partial_t B^e_0} \mathbf{N}^{eT} \bar{\mathbf{T}}^e dS \right\},
\end{aligned}
$$

where $\boldsymbol{A}$ is the element assemble operator, $\mathbf{N}^e$ is the element shape function matrix, and $\mathbf{B}^e$ is the element B-matrix. For the first approach, the force vector $\mathbf{f}^{cohe}$ can written as

$$
\mathbf{f}^{cohe} = - \mathop{\boldsymbol{A}}_{e=1}^{n^c_{elem}} \int_{S^e_c} \mathbf{N}^{eT} \mathbf{T}^{cohe}_e dS
$$

while for the second approach,

$$
\mathbf{f}^{cohe} = \mathop{\boldsymbol{A}}_{e=1}^{n^c_{elem}} \left\{ \int_{C^e_0} \left[\mathbf{B}^{eT} \mathbf{P}^e_c(\mathbf{d}) + \mathbf{C}^{eT} \mathbf{Q}^e_c(\mathbf{d}) \right] dV \right\},
$$

where the second order stain-displacement matrix $\mathbf{C}^e := \frac{\partial^2 \mathbf{N}^e}{\partial \mathbf{X} \otimes \partial \mathbf{X}}$.

The Newmark-β method with $\beta = 0, \gamma = 0.5$[31] is adopted in the explicit time integration,

$$\begin{aligned} \mathbf{v}_{n+\frac{1}{2}} &= \mathbf{v}_{n-\frac{1}{2}} + \mathbf{a}_n \Delta t_n \\ \mathbf{d}_{n+1} &= \mathbf{d}_n + \mathbf{v}_{n+\frac{1}{2}} \Delta t_n \\ \mathbf{a}_{n+1} &= \mathbf{M}^{-1}(\mathbf{f}^{ext} - \mathbf{f}^{int} - \mathbf{f}^{cohe}), \end{aligned} \tag{20}$$

where $\mathbf{d}_n$ is the displacement field at the time step at time step n, $\mathbf{v}_{n-\frac{1}{2}}$ is the half step velocity field at the time step $n - \frac{1}{2}$, and $\mathbf{a}_n$ is the acceleration field at the time step n. The subscript n and $n+1$ denote the quantities evaluated at time t_n and t_{n+1}. After the displacement field is updated, the stress measures can then be updated correspondingly, and hence the force vectors and acceleration $\mathbf{a}_{n+1}$ in the next time step are obtained.

5. Numerical Simulations

In this section, numerical examples are presented, to demonstrate the capability of the proposed process zone model, in the simulations of crack propagation and spall fracture in polycrystalline solids.

5.1. *Fracture in polycrystalline material*

In this example, a two-dimensional plate with dimension (2 mm × 2 mm) is subjected to unilateral tension in Y direction (see Fig. 5). Using the cohesive FEM,

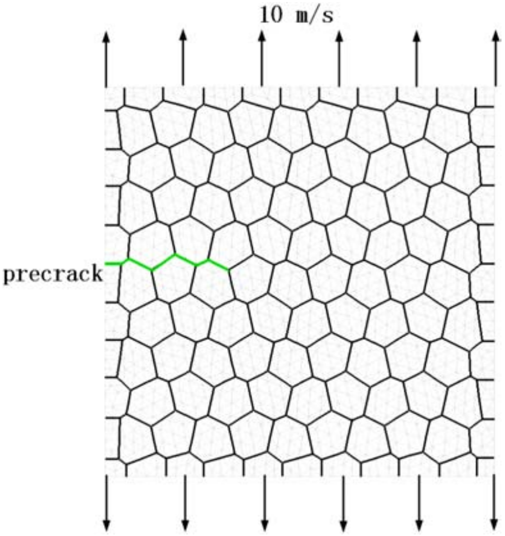

Fig. 5. Schematic of the unilateral tension.

the plate is discretized into 121 grains and 2376 bulk elements (see Fig. 5), which ultimately contains 3484 cohesive elements in the system. A pre-crack is set along several grain boundaries on the left side of the plate. The time step is chosen to be $\Delta t = 1 \times 10^{-10}$ s. in the simulation. It is postulated that with different relative strength of the cohesive zones between bulk elements in the grains and those on the grain boundary, the crack path might be different. In this work, strength of the cohesive zone is represented by the depth of the depletion potential. Two different cases are considered in this example, i.e, $\epsilon^{gb}_{depl} = \epsilon^{g}_{depl}$ and $\epsilon^{gb}_{depl} = 0.5\epsilon^{g}_{depl}$, where ϵ^{g}_{depl} denotes the width of the depletion potential in the process zones within the grains and ϵ^{gb}_{depl} represents the width of the depletion potential in the process zones on the grain boundaries. We first implemented the method using the second

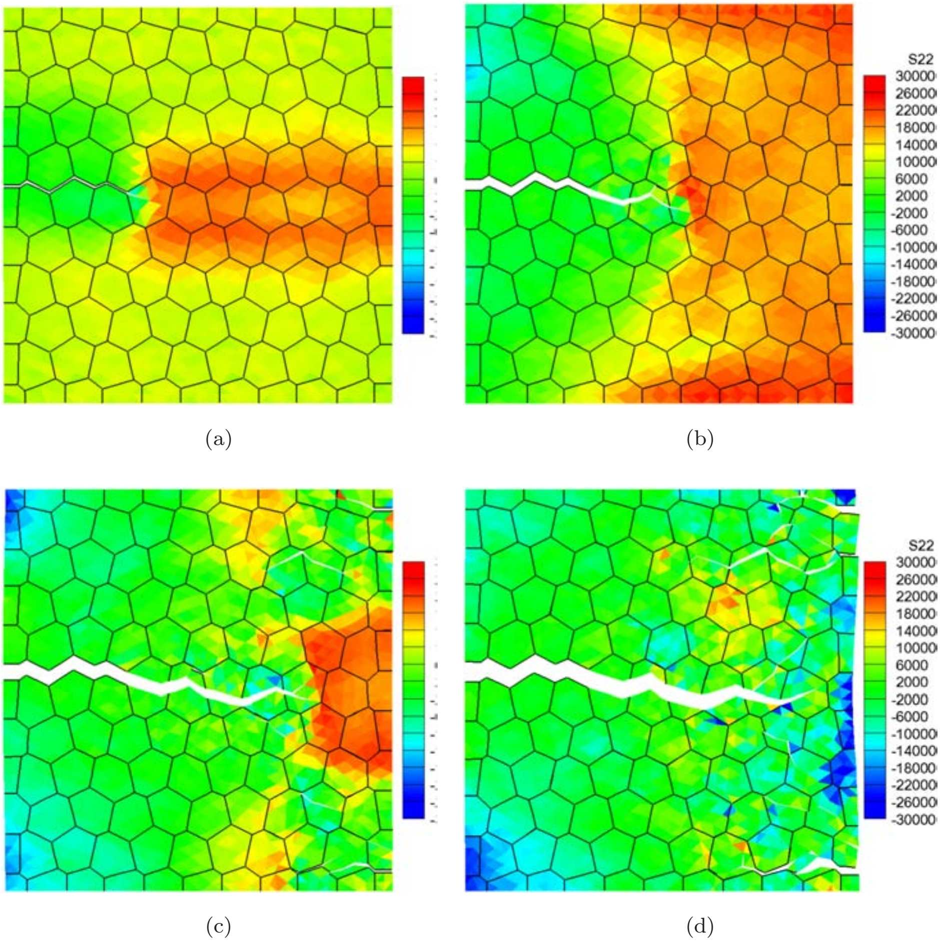

(a) (b) (c) (d)

Fig. 6. Crack propagates through grains: (a) $t = 1.5\,\mu$s; (b) $t = 2.5\,\mu$s; (c) $t = 3.5\,\mu$s; (d) $t = 4.5\,\mu$s. The simulation is conducted using the second approach.

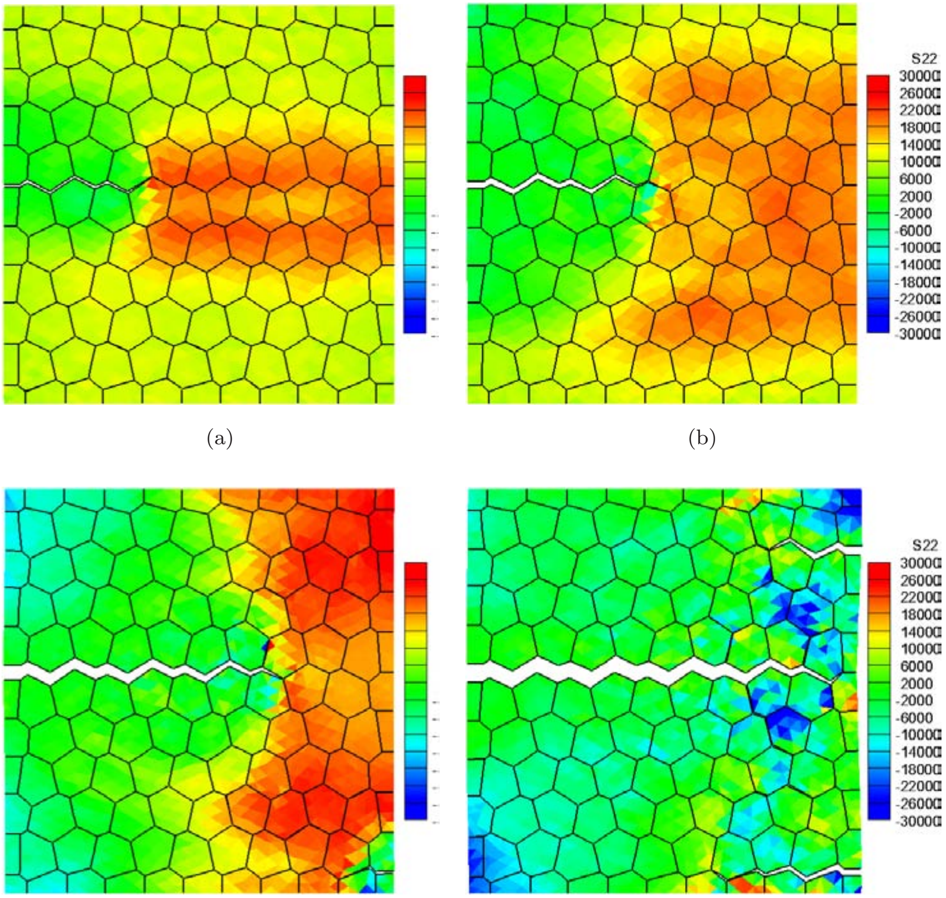

(a) (b)

(c) (d)

Fig. 7. Crack propagates along grain boundaries: (a) $t = 1.5\,\mu$s; (b) $t = 2.0\,\mu$s; (c) $t = 3.0\,\mu$s; (d) $t = 4.0\,\mu$s. The simulation is conducted using the second approach.

approach. From Fig. 6, it can be seen that crack propagated through grains for the first case. However, for the second one, the crack path followed closely along the grain boundaries as shown in Fig. 7.

5.2. *Comparison studies*

To evaluate the numerical performance of the proposed approaches, two subsequent simulations with exact the same parameters and problem setup of the trans-granular crack propagation are carried out. The second simulation is conducted using the first approach, whose result is shown in Fig. 8. The last example, as a comparison, is implemented by assuming uniform deformation within the cohesive zones, with the result given in Fig. 9. As one can see, the results from two approaches

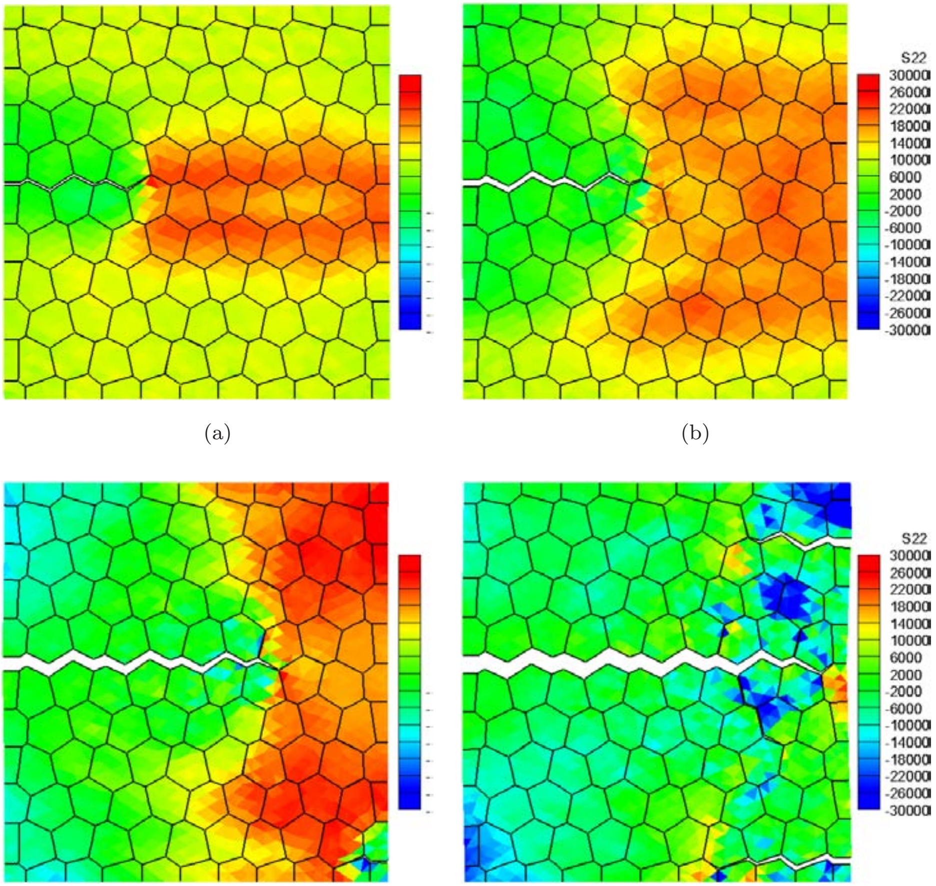

(a) (b)

(c) (d)

Fig. 8. Crack propagates along the grain boundaries: (a) $t = 1.5\,\mu$s; (b) $t = 2.0\,\mu$s; (c) $t = 3.0\,\mu$s; (d) $t = 4.0\,\mu$s. The simulation is conducted using the first approach.

proposed are almost the same, but the one based on the assumption of uniform deformation is quite different. As a comparison, the results from the three different methods is shown in Fig. 10. By assuming that the deformation in the cohesive zone is uniform, the crack surfaces become very wavy as the propagations progress. This can be attributed to several factors. First, the first order Cauchy-Born rule applied cannot correctly represent the nonuniform deformations in the cohesive zone. Second, because of the uniform deformation assumption, zero energy modes (especially the hour-glass modes) are present during the corresponding simulations. On the contrary, the approaches the second order Cauchy-Born rule and adopting a reduced two-point integration in the cohesive zone region provide very smooth and robust results. Therefore, in practical application, the two proposed approaches are recommended.

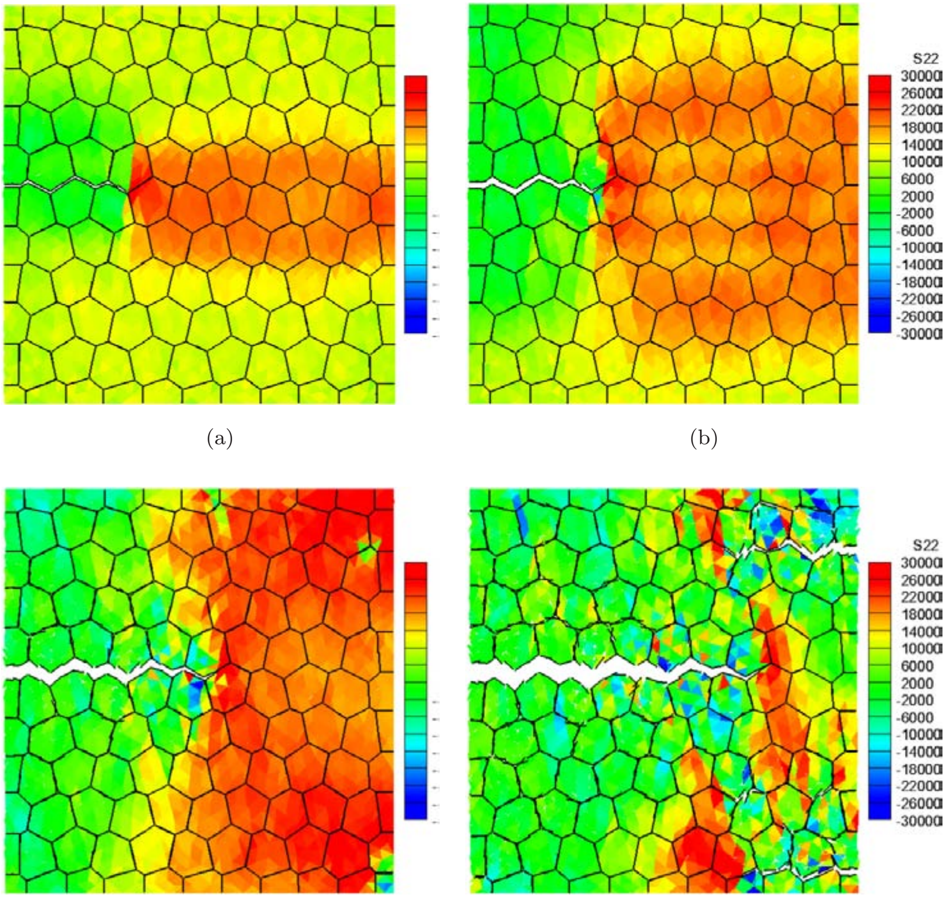

(a) (b)

(c) (d)

Fig. 9. Crack propagates along grain boundaries: (a) $t = 1.5\,\mu$s; (b) $t = 2.0\,\mu$s; (c) $t = 3.0\,\mu$s; (d) $t = 4.0\,\mu$s. The simulation is conducted by assuming the deformation is uniform in the cohesive zone.

5.3. *Convergence test*

In general, the results obtained from the simulations based on cohesive zone model are size-dependent. To test the effects of mesh size in multiscale process zone method, a unilateral tension test is implemented with four different meshes. Same as the previous simulation, the specimen is a two-dimension plate with dimension $(0.02\,\text{mm} \times 0.02\,\text{mm})$, which contains 121 grains. Constant velocity boundary condition is applied on both top and bottom edges. The ration ρ between average element size and average grain size is used to define mesh density. The three different meshes, corresponding to $\rho = 0.5, 0.2, 0.1, 0.05$, are used, as shown in Fig. 11. In addition, the cohesive strength in the cohesive zones inside grains are set to be

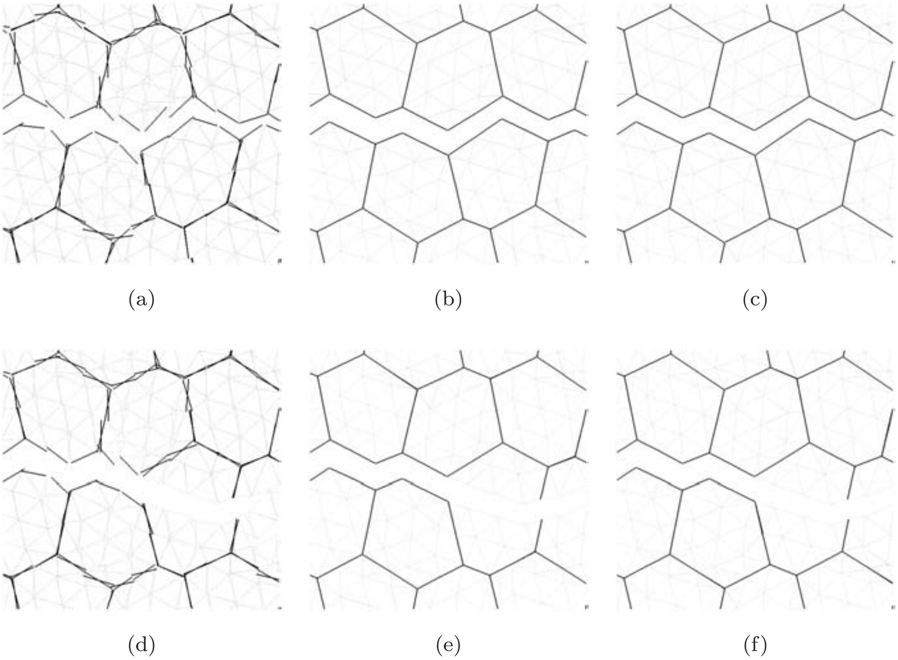

Fig. 10. Crack surface morphologies at $t = 3.0\,\mu$s. (a) Trans-granular — uniform deformation in the cohesive zone; (b) Trans-granular — the second approach; (c) trans-granular — the first approach; (d) inter-granular — uniform deformation in the cohesive zone; (e) inter-granular — the second approach; (f) inter-granular — the first approach.

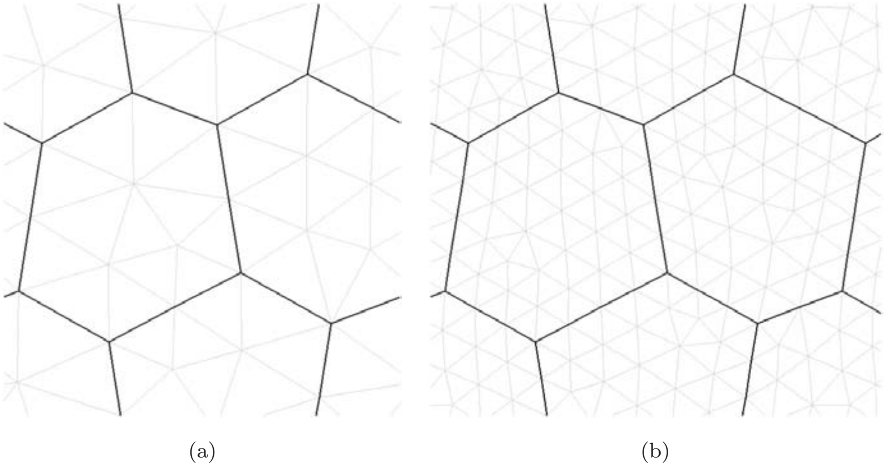

Fig. 11. Different meshes over grains: (a) Mesh 1: $\rho = 0.5$. (b) Mesh 2: $\rho = 0.2$. (c) Mesh 3: $\rho = 0.1$. (d) Mesh 4: $\rho = 0.05$.

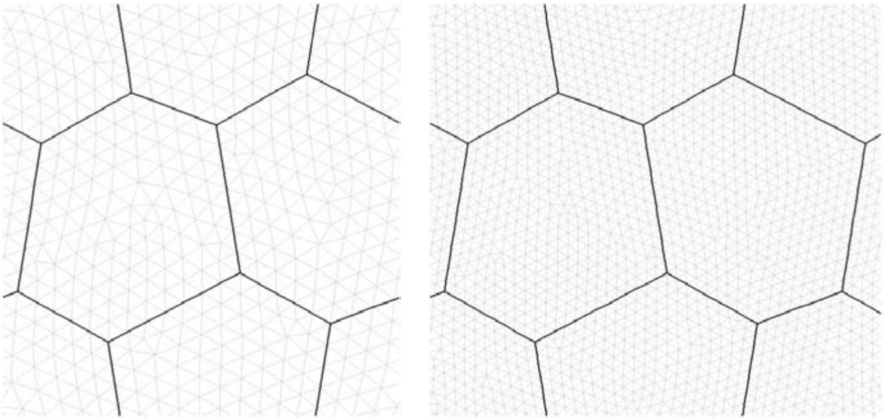
(c) (d)

Fig. 11. (*Continued*)

stronger than that of the grain boundary, which shall lead to transgranular crack propagations. In all the four tests, the second approach is adopted. Figure 12 shows the crack propagations in the specimen. It can been clearly seen that the crack propagates along same grain boundaries although mesh density varies so much.

To further check the convergence of the numerical simulation, the total reaction forces r_f^i on top edge are calculated in each mesh size, and they are plotted in Fig. 13. It can been seen that the evolutions of the reaction forces for the four different meshes are very close to each other and the gap between the curves from

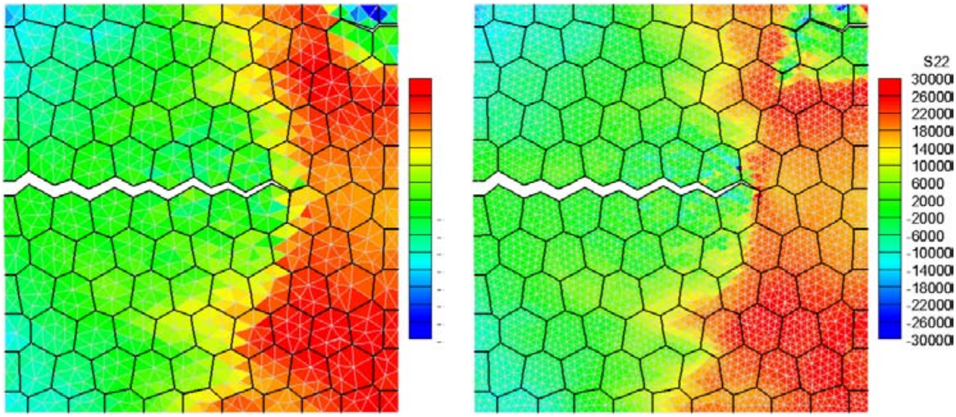

(a) (b)

Fig. 12. Crack surfaces calculated by different meshes: (a) Mesh 1: $\rho = 0.5$. (b) Mesh 2: $\rho = 0.2$. (c) Mesh 3: $\rho = 0.1$. (d) Mesh 4: $\rho = 0.05$.

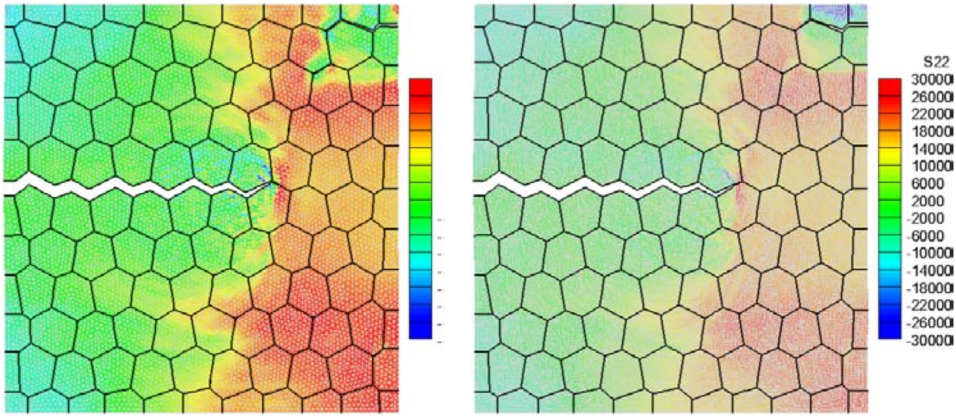

(c) (d)

Fig. 12. (*Continued*)

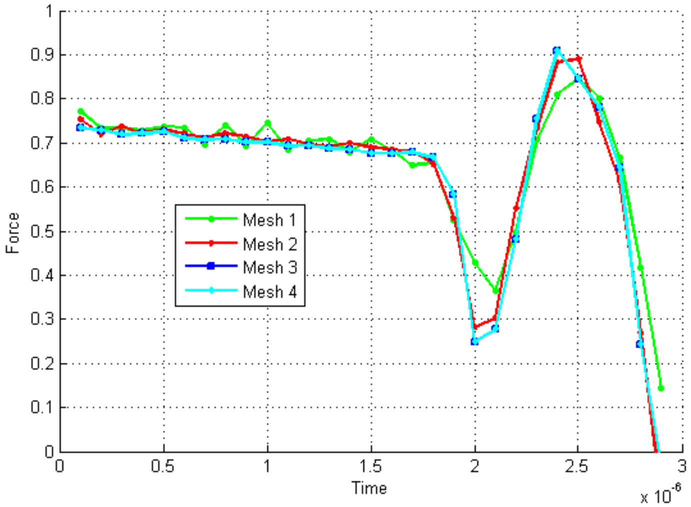

Fig. 13. Reaction force varies along time.

two consecutive meshes becomes smaller and smaller as the mesh size decreases, which proves the convergence and robustness of the proposed model.

5.4. *Simulations of spall fracture under high speed impact*

In this example, numerical simulations have been carried out to simulate spall fractures under high-speed impact, which is a very difficult task that has been elusive to many existing numerical methods.[32–34] As shown in Fig. 14, the left is a rigid block with impact velocity $v = 200\,\mathrm{m/s}$, the right is the target block

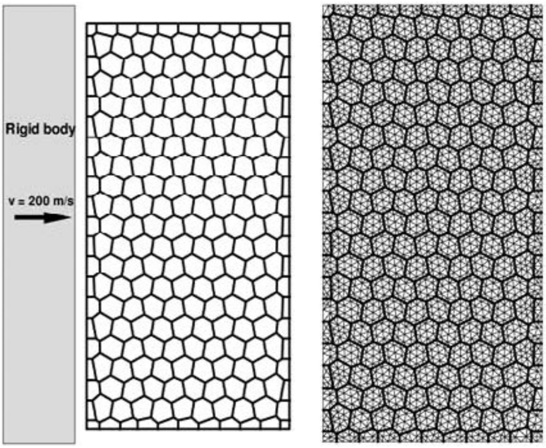

(a) (b)

Fig. 14. Example of high speed impact: (a) Sketch of impact model. (b) Mesh of the plate.

with dimension 1 mm × 2 mm. In the simulation, the target block is discretized into 861 grains and 4838 triangular bulk elements, which gives rise to a total of 7148 cohesive elements. As in the first example, the lattice orientations for the bulk element are randomly distributed based on the different grains and the orientation of the cohesive zone is set to be the average of the two sandwiching bulk elements. The second approach is adopted and the simulation time step is chosen as $\Delta t = 1 \times 10^{-10}$ s. The method in Ref. 35 is employed to enforce the exact impenetrability condition in a single time step. It is observed that the wave propagation initially starts from the contact point and bounces back after reaches the opposite boundary. Using different relative strength of the cohesive element in the bulk and that on the grain boundary, spall fractures under high speed impacts have been successfully captured, as shown in Figs. 15 and 16.

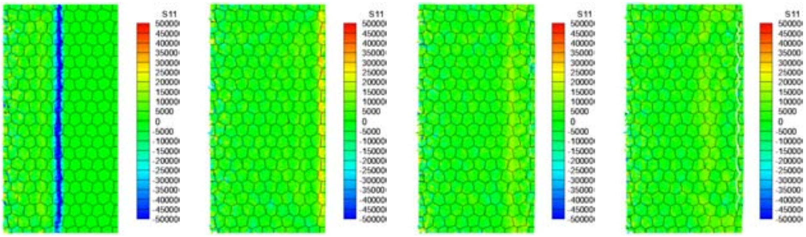

(a) (b) (c) (d)

Fig. 15. Spall fracture propagates through grains: (a) $t = 0.5\,\mu$s; (b) $t = 1.0\,\mu$s; (c) $t = 1.2\,\mu$s; (d) $t = 1.4\,\mu$s.

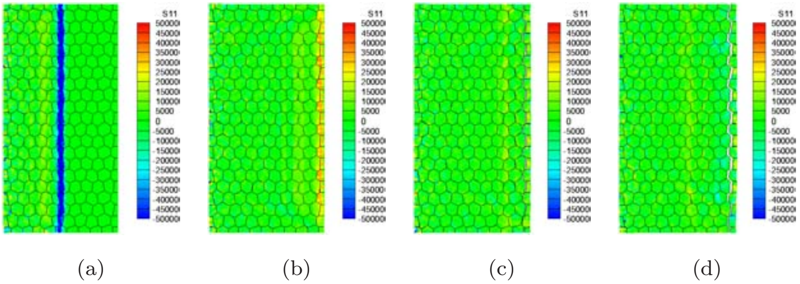

Fig. 16. Spall fracture propagates along grain boundaries: (a) $t = 0.5\,\mu$s; (b) $t = 1.0\,\mu$s; (c) $t = 1.2\,\mu$s; (d) $t = 1.4\,\mu$s.

6. Discussions

In this work, a multiscale process zone model is employed to simulate dynamic fractures in ploycrystalline solids. The multiscale process model makes use of the atomistic information, such as lattice structure and orientation in the polycrystalline solid to characterize the constitutive relations. The multiscale process zone model formulates the interface depletion potential to represent the mesoscale material properties in the process zone. Two different approaches in characterizing the process zone are compared: (1) the depletion potential approach, and (2) the higher order Cauchy-Born rule approach. By adopting the second order Cauchy-Born rule and the reduced integration technique in the process zone, fracture of polycrystalline solids with great accuracy and flexibility are demonstrated.

First by using the second approach, it is shown that the multiscale process zone model can predict both inter-granular and trans-granular fractures and their transitions. A comparison study of the crack surface morphologies of the simulation based on the two approached have been carried out. It is revealed that the approach with higher order Cauchy-Born rule and the reduced integration (2×1) in the process zone provides much better numerical accuracy and computing performance. Moreover, the second order Cauchy-Born is better in capturing the highly nonuniform deformation inside the process zone. On the other hand, the reduced integration is needed to eliminate the zero-energy modes while at the same time, to maintain the computation accuracy. In addition, based on the simulation results from the consecutive refinements of the same numerical test, one may find that the proposed model is size-independent in the simulation of crack propagations along the grain boundaries.

Second, spall fracture induced by high-speed impact loads is captured using the proposed model, without adding any artificial viscosities. The numerical simulation results are in good qualitatively agreement with the experimental observation.

The main difference between the multiscale process zone model and the conventional cohesive finite element method is how to construct interfacial surface cohesive potential. In the conventional cohesive model, the descriptions of the cohesive zone and the bulk element are some what disjointed. In the cohesive zone model, the empirical cohesive traction-separation relation is imposed, without any consideration of the bulk constitutive relation. In fact, the prescribed cohesive traction-separation relation is fixed in the sense that it does not take into account some most important physical characteristics of interfacial fracture, such as interphase orientation, its orientation difference with adjacent bulk elements, and interface micro-structures, etc. In the conventional cohesive zone model, the empirical interface cohesive laws are employed to model every cohesive zones for any arbitrary orientation, implicitly assuming material isotropy for every interfaces with arbitrary orientations, which is the main reason why we have so many difficulties in practice to match its results with experimental results. Whereas in the multiscale process zone model, the only objective constitutive relation is the bulk constitutive relation. The interface constitutive relation is obtained based on that in the bulk process zone, which varies from interface to interface. Moreover, by adopting the second order Cauchy-Born rule in the process zone, the model can better characterize the highly nonuniform deformation, making the model more realistic. It is because of these differences that the multiscale process zone model proves to be a better approach in simulation of fractures in polycrystalline solids.

Acknowledgments

Fan is partially supported by a fellowship from Chinese Scholar Council (CSC) and Shi is supported by a fellowship from the Faculty Training Project by Shanghai City Municipal Education Commission. There supports are gratefully acknowledged.

References

1. A. G. Crocker, P. E. J. Flewitt and G. E. Smith, Computational modelling of fracture in polycrystalline materials, *Int. Mater. Rev.* **50** (2005) 99–125.
2. W. A. Counts, M. Friák, D. Raabe and J. Neugebauer, Using *ab initio* calculations in designing bcc MgLi alloys for ultra-lightweight applications, *Acta Mater.* **57** (2009) 69–76.
3. V. Yamakov, D. Wolf, S. R. Phillpot, A. K. Mukherjee and H. Gleiter, Deformation-mechanism map for nanocrystalline metals by molecular-dynamics simulation, *Nature Mater.* **3** (2004) 43–47.
4. O. M. Ivasishin, S. V. Shevchenko, N. L. Vasiliev and S. L. Semiatin, A 3D Monte-Carlo (Potts) model for recrystallization and grain growth in polycrystalline materials, *Mater. Sci. Eng. A* **433** (2006) 216–232.
5. Z. P. Bazant, F. Asce, B. H. Oh and A. M. Asce, Microplane model for progressive fracture of concrete and rock, *J. Eng. Mech.* **111** (1985) 559–582.
6. F. L. Addessio and J. N. Johnson, A constitutive model for the dynamic response of brittle materials, *J. Appl. Phys.* **67** (1990) 3275.
7. D. R. Curran, L. Seaman, T. Cooper and D. A. Shockey, Micromechanical model for communition and granular flow of brittle material under high strain rate application to penetration of ceramic targets, *J. Impact Eng.* **13** (1993) 53–83.
8. H. D. Espinosa, On the dynamic shear resistance of ceramic composites and its dependence on applied multiaxial deformation, *Int. J. Solids Struct.* **32** (1995) 3105–3128.

9. X.-P. Xu and A. Needleman, Numerical simulations of fast crack growth in brittle solids, *J. Mech. Phys. Solids* **42** (1994) 1397–1434.
10. M. Ortiz and A. Pandolfi, Finite-deformation irreversible cohesive elements for three-dimensional crack-propagation analysis, *Int. J. Numer. Meth. Eng.* **44** (1999) 1267–1282.
11. G. N. Wells and L. J. Sluys, A new method for modelling cohesive cracks using finite elements, *Int. J. Numer. Meth. Eng.* **50** (2001) 2667–2682.
12. N. Moes and T. Belytschko, Extended finite element method for cohesive crack growth, *Frac. Eng. Mech.* **69** (2002) 813–833.
13. H. D. Espinosa and P. D. Zavattieri, A grain level model for the study of failure initiation and evolution in polycrystalline brittle materials, Part I: Theory and numerical implementation, *Mech. Mater.* **35** (2003) 333–364.
14. R. Duddu and H. Waisman, A temperature dependent creep damage model for polycrystalline ice, *Mech. Mater.* **46** (2012) 23–41.
15. R. A. Lebensohn, J. P. Escobedo, E. K. Cerreta, D. Dennis-Koller, C. A. Bronkhorst and J. F. Bingert, Modeling void growth in polycrystalline materials, *Acta Mater.* **61** (2013) 6918–6932.
16. A. Shojaei, G. Z. Voyiadjis and P. J. Tan, Viscoplastic constitutive theory for brittle to ductile damage in polycrystalline materials under dynamic loading, *Int. J. Plasticity*, **48** (2013) 125–151.
17. M. Paggi and P. Wriggers, A nonlocal cohesive zone model for finite thickness interfaces Part II: FE implementation and application to polycrystalline materials, *Comput. Mater. Sci.* **50** (2011) 1634–1643.
18. M. Paggi, E. Lehmann, C. Weber, A. Carpinteri, P. Wriggers and M. Schaper, A numerical investigation of the interplay between cohesive cracking and plasticity in polycrystalline materials, *Comput. Mater. Sci.* **77** (2013) 81–92.
19. G. K. Sfantos and M. H. Aliabadi, Multi-scale boundary element modelling of material degradation and fracture, *Comput. Meth. Appl. Mech. Eng.* **196** (2007) 1310–1329.
20. P. Van Houtte, A. K. Kanjarla, A. Van Bael, M. Seefeldt and L. Delannay, Multiscale modelling of the plastic anisotropy and deformation texture of polycrystalline materials, *Eur. J. Mech.-A/Solids*, **25** (2006) 634–648.
21. X. Zeng and S. Li, A multiscale cohesive zone model and simulations of fractures, *Comput. Meth. Appl. Mech. Eng.* **199** (2010) 547–556.
22. X. Zeng and S. Li, Application of a multiscale cohesive zone method to model composite materials, *Int. J. Multiscale Comput. Eng.* **10** (2012) 391–405.
23. M. He and S. Li, An embedded atom hyperelastic constitutive model and multiscale cohesive finite element method, *Comput. Mech.* **49** (2011) 337–355.
24. L. Liu and S. Li, A finite temperature multiscale interphase zone model and simulations of fracture, *J. Eng. Mater. Technol.* **134** (2012) 031014.
25. J. Qian and S. Li, Application of multiscale cohesive zone model to simulate fracture in polycrystalline solids, *J. Eng. Mater. Technol.* **133** (2011) 011010.
26. S. Li, X. Zeng, B. Ren, J. Qian, J. Zhang and A. K. Jha, An atomistic-based interphase zone model for crystalline solids, *Comput. Meth. Appl. Mech. Eng.* **229–232** (2012) 87–109.
27. S. Ghosh and Y. Liu, Voronoi cell finite element model based on micropolar theory of thermoelasticity for heterogeneous materials, *Int. J. Numer. Meth. Eng.* **38** (1994) 1361–1398.
28. J. E. Bolander and S. Saito, Fracture analyses using spring networks with random geometry, *Eng. Frac. Mech.* **61** (1998) 569–591.
29. J. Israelachvili, *Intermolecular and Surface Forces*, Academic Press, 1991.

30. T. J. Hughes, *The Finite Element Method*: *Linear Static and Dynamic Finite Element Analysis*. Courier Dover Publications, 2012.
31. T. Belytschko, J. S. Ong, W. K. Liu and J. M. Kennedy, Hourglass control in linear and nonlinear problems, *Comput. Meth. Appl. Mech. Eng.* **43** (1984) 251–276.
32. T. Antoun, L. Seaman, D. R. Curran and G. I. Kanel, *Spall Fracture* (Shock Wave and High Pressure Phenomena), Springer, 2003.
33. J. D. Clayton, Modeling dynamic plasticity and spall fracture in high density polycrystalline alloys, *Int. J. Solids and Struct.* **42** (2005) 4613–4640.
34. B. Ren and S. Li, A three-dimensional atomistic-based process zone model simulation of fragmentation in polycrystalline solids, *Int. J. Numer. Meth. Eng.* **93** (2012) 989–1014.
35. T. J. R. Hughes, R. L. Taylor, J. L. Sackman, A. Curnier and W. Kanoknukulchai, A finite element method for a class of contact-impact problems, *Comput. Meth. Appl. Mech. Eng.* **8** (1976) 249–276.